DiVA
http://www.diva-portal.org

This is the published version of a paper published in *Science Advances*.

Citation for the original published paper (version of record):

Yalcin, S E., Legg, B A., Yesilbas, M., Malvankar, N S., Boily, J-F. (2020)
Direct observation of anisotropic growth of water films on minerals driven by defects and surface tension
Science Advances, 6(30): eaaz9708
https://doi.org/10.1126/sciadv.aaz9708

Access to the published version may require subscription.

N.B. When citing this work, cite the original published paper.

Permanent link to this version:
http://urn.kb.se/resolve?urn=urn:nbn:se:umu:diva-174045

SURFACE CHEMISTRY

Direct observation of anisotropic growth of water films on minerals driven by defects and surface tension

Sibel Ebru Yalcin[1,2]*, Benjamin A. Legg[3,4], Merve Yeşilbaş[5†], Nikhil S. Malvankar[1,2]*, Jean-François Boily[5]*

Copyright © 2020 The Authors, some rights reserved; exclusive licensee American Association for the Advancement of Science. No claim to original U.S. Government Works. Distributed under a Creative Commons Attribution NonCommercial License 4.0 (CC BY-NC).

Knowledge of the occurrences of water films on minerals is critical for global biogeochemical and atmospheric processes, including element cycling and ice nucleation. The underlying mechanisms controlling water film growth are, however, misunderstood. Using infrared nanospectroscopy, amplitude-modulated atomic force microscopy, and molecular simulations, we show how water films grow from water vapor on hydrophilic mineral nanoparticles. We imaged films with up to four water layers that grow anisotropically over a single face. Growth usually begins from the near edges of a face where defects preferentially capture water vapor. Thicker films produced by condensation cooling completely engulf nanoparticles and form thicker menisci over defects. The high surface tension of water smooths film surfaces and produces films of inhomogeneous thickness. Nanoscale topography and film surface energy thereby control anisotropic distributions and thicknesses of water films on hydrophilic mineral nanoparticles.

INTRODUCTION

Hydrophilic minerals exposed to water vapor are covered by nanometer- to micrometer-thick water films (Fig. 1A) (*1*). These films are intrinsically tied to the availability and transport of water in environmental (*2*) and atmospheric (*3*) processes. The nano- to microscale solvation environments (*4*) of mineral-supported water films impact the global cycling of nutrients and elements in terrestrial environments, control microscale variations in soil pH (*2*), and are even crucial for the survival of microorganisms and other life forms in arid environments (*5*). Water and ice films additionally play an essential role in atmospheric cloud formation phenomena (*3*) and thereby the global climate (*6*) and climate geoengineering (*7*). As water films are continuously responsive to variations in atmospheric humidity, determining their formation and removal mechanisms on minerals is crucial for identifying the occurrences and forms of water and the reactions that these water films host in nature.

Water films grow on minerals via adhesive mineral-water and cohesive water-water interactions (*8*, *9*). Adhesive interactions of the adsorption regime (Fig. 1B) predominate under atmospheres of low relative humidity (RH), producing water nanoclusters and/or thin water films of no more than a few monolayers. One monolayer corresponds to a density of ~10 to 12 H_2O/nm^2 on oxide minerals. Cohesive interactions trigger a condensation regime (Fig. 1B) causing water clusters to coalesce, thin films to grow into thicker overlayers, and fill surface roughness features and interparticle pores. Water adsorption isotherm models (*8*, *9*) can account for such regimes (Fig. 1B), yet cannot provide insight into the molecular-level and nanoscale controls on film growth. Spectroscopic studies (*1*, *4*, *10*) have confirmed that mineral-bound films expose properties akin to those of liquid water but are also limited in providing information on the spatial distributions of these films. While atomic and polarization force microscopy have revealed nanoscale structures of films at various surfaces (*11*–*15*), these methods can only infer on the presence of water through indirect means. As such, more direct and chemically sensitive probes are needed to advance ideas on water film growth on minerals. These can be especially useful for imaging spatial distributions of water accessible to (biogeo)chemical reactions and microorganisms in nature.

In this study, we overcome these hurdles by correlating spatial distributions of water films with the nanoscale surface chemistry of minerals by simultaneously analyzing chemical activity and mineral topography. We achieved this by directly visualizing water films on individual mineral nanoparticles with (i) infrared (IR) nanospectroscopy (Fig. 2) tuned to the bending mode of water (*16*) and (ii) amplitude-modulated atomic force microscopy (AM-AFM) providing high-resolution topographic imaging and estimating film thickness. Atmospheric RH levels were limited to ranges of negligible tip-sample capillary condensation indicated by previous studies (*13*, *17*, *18*). Water films were imaged on single gibbsite [γ-$Al(OH_3)$] nanoparticles (fig. S1), which are highly relevant to nature and technology. The prominent (001) basal face of these nanoparticles not only lends well to AFM imaging (*19*, *20*) but also hosts some of the thinnest water films that can be formed on hydrophilic minerals. (*21*) Nanometric defects, commonly expressed as stepped edges on gibbsite (*19*, *20*), are sources of greater hydrophilicity as they expose varied types of hydroxo groups and can trigger condensation well below the dew point of water, as can be understood by the Kelvin effect (*22*).

Direct imaging of low densities of water films (adsorption regime, ≤25% RH) was achieved by scattering-type scanning near-field optical microscopy (IR *s*-SNOM) (Figs. 2 and 3). The high chemical sensitivity of this IR nanospectroscopic technique (*23*) enabled detection of localized accumulations of water films. Lack of tip-sample capillary condensation was confirmed further by additional IR *s*-SNOM imaging of hydrophobic holmium oxide (Ho_2O_3) nanoparticles (*24*) under the same conditions. Water films formed at higher water loadings (condensation regime, >40% RH) were imaged

[1]Department of Molecular Biophysics and Biochemistry, Yale University, New Haven, CT 06511, USA. [2]Microbial Sciences Institute, Yale University, West Haven, CT 06516, USA. [3]Physical Sciences Division, Pacific Northwest National Laboratory, Richland, WA 99352, USA. [4]Department of Materials Science and Engineering, University of Washington, Seattle, WA 98195, USA. [5]Department of Chemistry, Umeå University, SE-901 87 Umeå, Sweden.
*Corresponding author. Email: jean-francois.boily@umu.se (J.-F.B.); sibel.yalcin@yale.edu (S.E.Y.); nikhil.malvankar@yale.edu (N.S.M.)
†Present address: Carl Sagan Center, SETI Institute, Mountain View, CA 94043, USA.

Downloaded from http://advances.sciencemag.org/ on August 13, 2020

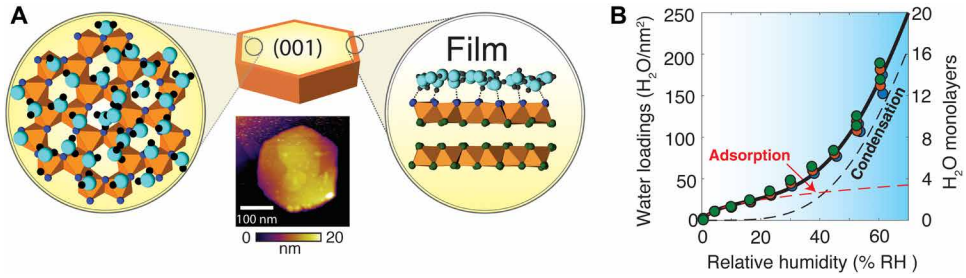

Fig. 1. Water adsorption and condensation on gibbsite nanoparticles. (**A**) Schematic representation of a water film on the basal (001) face of a single gibbsite (γ-Al(OH)$_3$) nanoparticle. Molecular structures are taken from a snapshot of a selected portion of a pristine simulation cell (see Fig. 5 at 12 H_2O/nm^2) by molecular dynamics (MD). Water molecules (turquoise O, black H) form networks of hydrogen bonds (dashed line) with surface hydroxo groups of the (001) surface. AFM imaging revealed the morphology, crystal habit, topographical variations, and defects of the gibbsite nanoparticles under study (see fig. S1 for additional images). (**B**) Water vapor adsorption isotherms (25°C) on gibbsite nanoparticles measured by quartz crystal microgravimetry. A modified water binding model (Eq. 2; see Materials and Methods) predicts adsorption data (here collected in triplicates) in terms of an adsorption regime at low % RH and of a condensation regime at high % RH.

by AM-AFM, and their thickness was estimated by force nanospectroscopy (Fig. 4). Both methods revealed anisotropic distributions of water films on gibbsite. Possible causes of this anisotropy were investigated by molecular simulations of single nanometric gibbsite nanoparticles (Fig. 5). Simulations indicated that surface defects drive water growth into preferential zones at low water loadings. Once these defects are swamped by a sufficiently thick water layer, the drive for film growth is dominated by the high surface tension of water, which smooths the film surface over the entire particle. Smoothing drives higher water loadings over the middle portion of the basal face and over deeper defects while relatively depleting densities near particle edges or flat faces near defects (Figs. 2D and Fig. 5). Our findings provide previously unknown insight into nanoscale processes driving water film formation on oxide mineral nanoparticles.

RESULTS

IR *s*-SNOM imaging revealed anisotropic water film growth

IR *s*-SNOM imaging of water films (Fig. 2) was achieved using a wavelength tunable quantum cascade laser (QCL; bandwidth, <1 cm^{-1}) focused to an AFM tip apex that reduces the spatial resolution down to the nanoscale (tip radius, ~25 nm) (Fig. 2A). The IR *s*-SNOM system was incorporated to one arm of an interferometer that operates in a two-phase homodyne mode (*25*). This interferometric imaging approach isolated and amplified the tip-scattered near-field signal with respect to the far-field background (Fig. 2A). The AFM tip used in this setup was sufficiently sensitive (*16*, *25*–*27*) to detect nanometric water films, as even a single monolayer of water (~10 to 12 H_2O/nm^2) on gibbsite (*21*) should correspond to ~19,000 to 23,000 oscillators.

To detect water on gibbsite, we tuned the QCL to the bending mode (ν_2) of water (*16*). An independent set of Fourier transform IR (FTIR) spectroscopy measurements confirmed that this spectral region responds uniquely to water films bound to gibbsite nanoparticles (Fig. 2B, black line, and fig. S2). The same spectral shape was also reproduced through our nanoscale IR *s*-SNOM studies (Fig. 2B, blue dots) on individual gibbsite minerals by collecting SNOM images with the QCL tuned at 13 different frequencies between 1580 and 1700 cm^{-1} (fig. S6). The agreement of the SNOM phase with FTIR results (Fig. 2B) confirmed that our nanoscale imaging approach was solely sensitive to these water films. The great majority of IR *s*-SNOM images collected for this work were achieved with the QCL tuned at 1630 cm^{-1}, as it corresponds to both an absorbance high for water films and a low between the finer lines of unadsorbed water vapor (fig. S3). In all cases, IR *s*-SNOM recorded both AFM topography (Fig. 2, C and D) and SNOM phase images (Fig. 2D and figs. S4 to S8) to simultaneously visualize topographical and chemical changes resulting from water film growth.

Intrinsic IR *s*-SNOM phases, corresponding to optical absorption properties, were obtained from images of gibbsite nanoparticles exposed to N_2(g) at preselected levels of RH at 25°C (Fig. 2D). The signals were averaged over a region of the gibbsite particle surface and corrected for the small background originating from the gold substrate (*25*). All of our SNOM images (Fig. 2D and figs. S4 to S8) indicate that water was localized only over gibbsite surfaces and not on the gold substrate (e.g., fig. S4). Images revealed that films grew from a single area at low RH and progressively covered the surface at higher RH. This anisotropic growth was independent of SNOM scan direction and was reversible when RH was lowered back to 0% (fig. S7). We discard tip-sample capillary condensation as a primary mechanism driving anisotropy given previous works (*13*, *17*, *18*) supporting this concept for AFM measurements under low RH. This was confirmed further in an additional set of IR *s*-SNOM phase images of hydrophobic holmium oxide (Ho_2O_3) nanoparticles (*24*) showing little water uptake (fig. S9 and Fig. 3A). The SNOM signal increases proportionally to RH only for gibbsite (Fig. 2), ensuring that mineral topography does not interfere with the SNOM signal.

IR *s*-SNOM phase values for all images collected for this work were numerically integrated and normalized over the area of the gibbsite particles identified by SNOM topography (Fig. 3A). Values for gibbsite systematically increased with humidity and were directly correlated (Fig. 3B) to microgravimetrically derived water loadings (Fig. 1B). This correlation was obtained by taking water loadings at every RH at which SNOM phase values were calculated. Here, assuming an equal distribution of water loadings on all crystallographic faces of the particles, the correlation suggests that IR *s*-SNOM imaged, on average, up to ~40 H_2O molecules per square nanometer under the adsorption regime. The data for one adsorption-desorption cycle (blue closed and open squares of Fig. 3) also display hysteresis, which could potentially be related to the different spatial distributions adopted by the water films during desorption (fig. S7). Overall, this correlation between IR *s*-SNOM phase values and microgravimetrically derived

Downloaded from http://advances.sciencemag.org/ on August 13, 2020

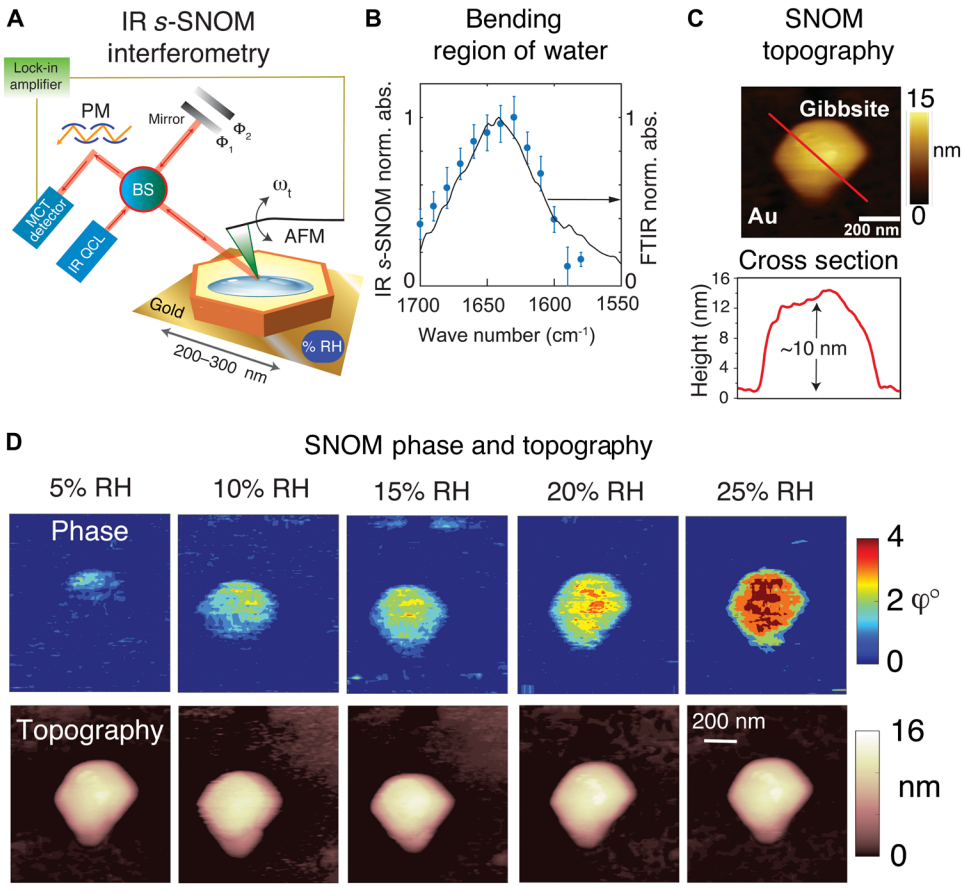

Fig. 2. IR nanospectroscopy reveals anisotropic growth of water film on gibbsite under the adsorption regime. IR *s*-SNOM images of gibbsite nanoparticles exposed to 0 to 25% RH (**A**) Schematic of IR *s*-SNOM operated in two-phase homodyne detection (see Materials and Methods). BS, beam splitter; PM, parabolic mirror; MCT, mercury cadmium telluride. (**B**) Normalized absorbance of IR *s*-SNOM phase (blue dots) over a gibbsite particle exposed to ambient atmosphere. Values were obtained from SNOM phase images, with the QCL tuned between 1580 and 1700 cm^{-1}. This SNOM-derived spectrum aligns with a typical FTIR spectrum (black line) of water films on gibbsite (see also fig. S2). Both spectra were normalized for their respective absorbance maximum ('norm. abs.') in this spectral range to faciliate comparison. (**C**) SNOM topography of individual gibbsite nanoparticle and its corresponding height cross section for the red line, collected at 0% RH. (**D**) Representative IR *s*-SNOM phase images collected with the QCL tuned at 1630 cm^{-1} with their corresponding topography images, showing anisotropic growth of water film starting from one edge of the particle. See figs. S6 to S8 for additional sets of images of other gibbsite nanoparticles. See Fig. 3 (A and B) for integrated phase values over the area of the particles correlated by SNOM topography.

water loadings underscores the power of IR *s*-SNOM for imaging the spatial distribution of molecularly thin water films on minerals.

For gibbsite, these measurements implicate commonly observed stepped edges [Fig. 4 and fig. S1, and previous reports (*19*, *20*)] in the preferential capture of water and thereby in the anisotropic growth of water films. This falls in line with theory (*22*) predicting that nanometric roughness of the same scale as those observed by AFM should be preferentially filled by water at RH levels considered in this work. The greater reactivity of these stepped edges over other defects, such as those of the basal (001) face (Fig. 2C), could also be explained by differences in nanoscale topography controlling energetics of water condensation. Differences in defect site activity are better recognized in the ice nucleation literature (*28*), where only a minority of sites trigger ice formation. Thus, by revealing the involvement of stepped edges in forming water films at low RH, our imaging work offers a novel way for interpreting adsorption isotherm data (Fig. 1).

SNOM imaging (Fig. 2D) also shows that films formed at higher levels of humidity tend to entirely engulf single gibbsite particles, and that water loadings are higher in the central part of the basal face than near edges. In the next sections, AM-AFM will be used to image these thicker films, and molecular simulations will show how the surface tension of water provides another source for anisotropy by controlling film geometry.

AM-AFM resolved water film and menisci thickness

Thicker water films grown under the condensation regime were tracked by AM-AFM, a technique also capable of imaging water (nano)droplets (*29*–*31*). For these experiments, water films were formed on ~10-nm-thick gibbsite nanoparticles (Fig. 4, A and B) by condensation cooling of an atmosphere initially set to 40% RH at 30°C. Exposure of 40% RH at 30° or 20°C had no impact on topography and thereby on apparent height. The first evidence of water film growth was, however, observed at 10°C (Fig. 4, A to C), and considerably more at 4°C with a ~2.5-nm increase in apparent particle height. The resulting film was thicker near the stepped edges of the particle, indicating the formation of menisci (Fig. 4 and fig. S10; see fig. S11 for condensation in the chamber). After reheating to 30°C, the menisci

Downloaded from http://advances.sciencemag.org/ on August 13, 2020

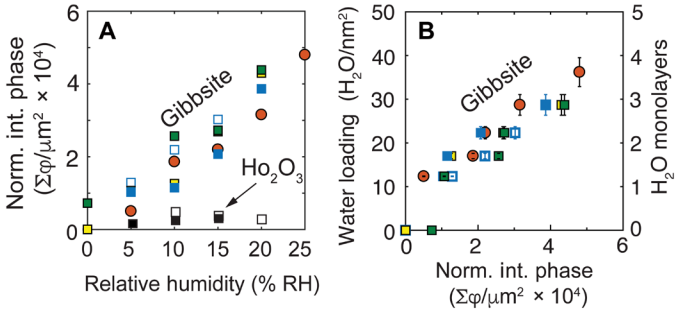

Fig. 3. IR nanospectroscopy scales with water loadings. (**A**) Normalized integrated phase over the entire area of the basal face of gibbsite exposed to 0 to 25% RH, taken from the images of Fig. 2D (orange circle) and fig. S7 (closed and open blue squares from one adsorption-desorption isotherm cycle), fig. S8 (yellow square), and one additional set images (green squares). Imaging of hydrophobic holmium oxide (Ho_2O_3) particles (black open and closed squares; fig. S9) reveals little water uptake. (**B**) Correlation between microgravimetrically derived water loadings (Fig. 1B) and the normalized integrated SNOM phase. This figure was made by relating the RH dependence of water loadings obtained by microgravimetry (Fig. 1B) to the RH dependence of the normalized integrated SNOM phase data (A). Thus, water loadings for every integrated SNOM phase value of (A) were taken from Fig. 1B for every given % RH. This relationship reveals a response ~1278 $\varphi/\mu m^2$ for each H_2O/nm^2, namely, ~782 H_2O/φ. It also shows that our SNOM imaging technique can successfully probe 1 to 4 water monolayers. Error bars are from the uncertainty in the microgravimetry measurements of Fig. 1B.

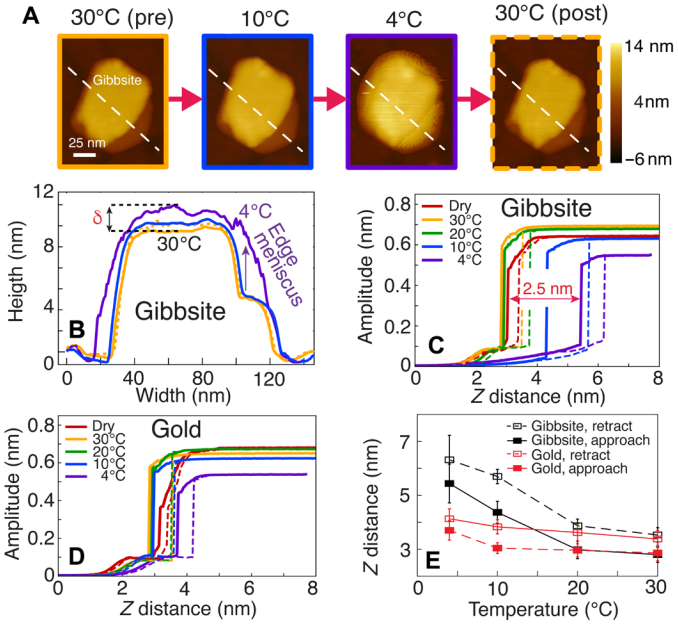

Fig. 4. AM-AFM reveals multilayered water films on gibbsite under the condensation regime. (**A**) AFM image sequence of gibbsite under humidified Ar(g) at 30°C (solid yellow frame), 10°C (blue frame), and 4°C (purple frame) and reheated to 30°C (dashed yellow frame). Imaging under dry Ar(g) confirmed that the gibbsite particle was ~10 nm thick. (**B**) Corresponding topographical cross sections. A step edge meniscus was observed at 4°C. Amplitude curves on (**C**) gibbsite and (**D**) bare gold under approach (solid lines) and retraction (dashed lines). (**E**) Jump distances during approach and retract on gibbsite and gold as a function of temperature. Hysteresis was observed, with jump-from-contact during retraction occurring at a greater distance than the jump-to-contact on approach. An increase in apparent particle thickness and the jump-to-contact distance at 4°C (δ ~ 2.5 nm) reveal the formation of ~9 water monolayers. Comparison of force-distance profiles confirmed that thick water films were formed on gibbsite, but not gold. Reversibility was observed in the gibbsite height (A and B) and in the tip approach/retract distances [(C) and table S1] after reheating the sample back to 30°C.

disappeared and the sample thickness returned to its original value of ~10 nm. This reversibility confirmed that the height increase was caused by a multilayered water film.

Because AM-AFM contrast formation mechanisms can be complex at the subnanometer scale (*29*, *32*), we resolved the humidity and temperature dependence on particle apparent height by force nanospectroscopy (Fig. 4C). These measurements provide insight into the sample-tip interaction forces (*33*) and present additional evidence that the apparent changes in particle thickness were caused by water films. In these experiments, an oscillating AFM tip was brought into contact with the surface while monitoring the oscillation amplitude, phase, and deflection (figs. S12 to S14). Force curves were obtained both on the gibbsite particle and on the neighboring gold substrate (Fig. 4D), which provided a control surface. Approaching the AFM tip to the surface under dry Ar(g) consistently induced a sudden decrease in amplitude at tip-sample distances of several nanometers. This was accompanied by a simultaneous negative jump in the deflection curve, referred to as "jump-to-contact" (solid lines in Fig. 4, C and D, and fig. S13). As the tip came into closer proximity to the surface, the oscillation amplitude was damped toward zero over the course of ~2 nm. Subsequent approach generated a positive deflection due to the tip contacting the surface. After achieving fixed deflection (designated to $Z = 0$), the tip was retracted from the surface and the amplitude recovered. This "jump-from-contact" (dashed lines of Fig. 4, C and D) exhibited hysteresis at greater Z distances (Fig. 4, C to E, and table S1). As this hysteresis was observed for both gibbsite and gold, even in dry environments, it was likely caused by mechanical interactions between the tip and the substrate.

As in the topography measurements, the force curves remained largely unchanged after introduction of humidified Ar(g) at 30° or 20°C. Growth of the thicker water films by cooling to 10° and 4°C induced substantial changes in the force curves (Fig. 4, C to E, and fig. S10). The jump events over gibbsite occurred at significantly larger distances at these temperatures and confirmed film thicknesses of ~1.5 nm (~5 monolayers) at 10°C and ~2.5 nm (~9 monolayers) at 4°C. Furthermore, as the postcontact amplitude damping proceeded more gradually, the tip was likely oscillating within a thick dissipative film rather than tapping against a hard surface. In comparison, the force curves displayed little change over the hydrophobic gold substrate, indicating that the changes were truly driven by a water film (Fig. 4, C and D, and table S1). Last, after reheating the gibbsite sample to 30°C, the jump distances returned to values that were similar to the original values (table S1).

Our AFM imaging and force spectroscopy consequently provide strong evidence for the reversible formation of a nanometer-scale multilayered water film in the condensation regime. Furthermore, the formation of menisci near stepped edges of the particles demonstrates the importance of defects on the anisotropic distributions of water. While these findings may be in apparent conflict with existing adsorption isotherm models (*8*) for isotropic film growth, they are supported further with the molecular-scale phenomena detailed in the following section.

Downloaded from http://advances.sciencemag.org/ on August 13, 2020

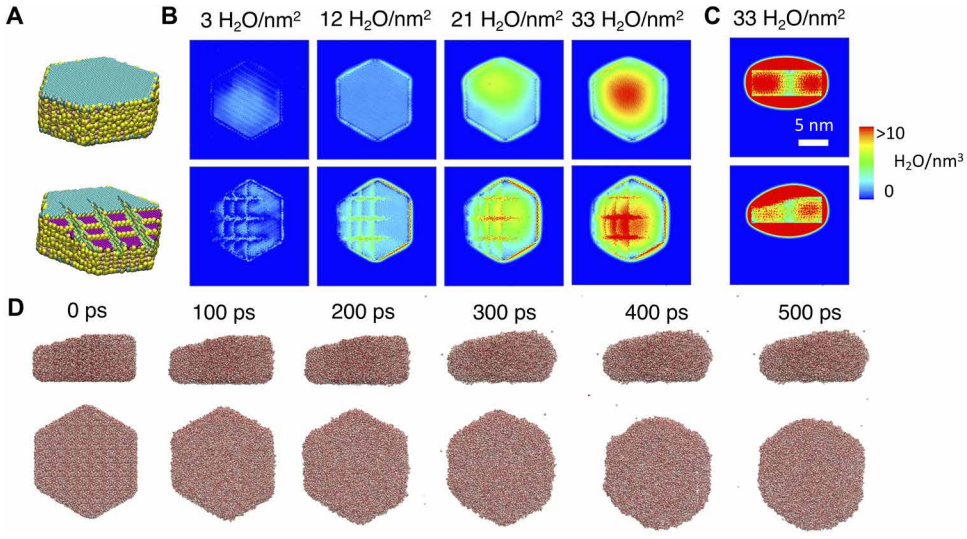

Fig. 5. MD show that the surface tension of water and mineral defects drive the anisotropic distribution of water on gibbsite nanoparticles. Simulations of 11.2 nm–by–13.4 nm–by–4.7 nm (**A**) pristine and roughened gibbsite particles covered in water films (3 to 33 H_2O/nm^2). Hydroxyl groups on different crystallographic faces and defect zones are color-coded. Water density (H_2O/nm^3) maps of the (**B**) (001) face (**C**) particle edge were generated from production run of at least 5000 ps performed at a time step of 0.5 fs in an NVT ensemble at 300 K. (**D**) Morphology of a film with 33 H_2O/nm^2 on the roughened particle [top row edge faces view; bottom row (001) face view] at selected simulation time. Films departed from the initial gibbsite morphology to decrease the total surface area, a means to minimize the surface energy (see fig. S15). This effectively increases water loadings over the central parts of the faces and depletes them at the edges. Simulations with roughened particles in the form of three 0.5-nm-thick steps and three grooves up to 1.0 nm deep revealed preferential water uptake to the defect sites first at low water loadings.

Defects and water surface tension control the spatial distributions of films

The driving forces for anisotropic water film growth were explored by molecular dynamics (MD) simulations of single nanometric gibbsite particles (Fig. 5). The simulated nanoparticles were of comparable crystal habit to those imaged for this work, yet they were ~20 to 30 times smaller due to computational demands. These were nonetheless sufficiently large to produce homogeneous water structures needed to understand water film growth (*34*).

Simulations were performed by equilibrating single pristine particles that were initially covered with water films of uniform thickness, with densities (3 to 33 H_2O/nm^2; Fig. 5A) well covering the experimental range of this work (Fig. 1B). Equilibration by MD retreated water molecules from particle edges and onto the central region of the basal face. This was driven by cohesive water-water interactions overcoming adhesive surface-water interactions, as also highlighted by similar work on talc surfaces (*35*). At larger water loadings, simulations revealed that water films covering the entire basal face smoothen to a point where excess free water completely engulfed the nanoparticle, resulting in an asymmetrically shaped nanodroplet (Fig. 5C). Simulated water densities were greater near the center of the particles in a comparable manner to IR *s*-SNOM images at 25% RH (Fig. 2D and figs. S4 and S6 to S8). This preferential accumulation at particle centers is facilitated in films of sufficiently high loadings where water can freely migrate laterally over a nanoparticle surface and is driven by the high surface tension of water.

In a second set of simulations, we analyzed the roles of defects (*19*, *20*) on the spatial distribution of water films (Fig. 5, B and C). For this work, an arbitrary set of defects was considered to simultaneously account for the effects of coexisting terraces, steps, and etches on water binding. Simulations at low water loadings revealed a preferential water uptake in defects. This can also explain our IR *s*-SNOM images at low RH (e.g., 5% RH in Fig. 2D), where water accumulates over one portion of the basal face, leaving the other portion relatively dehydrated. This preferential uptake is concomitantly driven by the establishment of a network of hydrogen bonds between water vapor and various reactive hydroxo groups at these defects (*36*). It even drains water away from flatter regions in the vicinity of these defects (Fig. 5B at 3 H_2O/nm^2) but then stops once defects are completely filled with water (Fig. 5B at 12 H_2O/nm^2). Greater water loadings then produced an asymmetrically shaped nanodroplet as in the defect-free particle. A time-resolved representation of film equilibration (Fig. 5D) at such high loadings illustrates salient changes in film morphology guided by a minimization in surface energy (fig. S15), especially at edges where interfacial curvature is largest. Thus, these two concurrent factors (defects and surface tension) drive water film growth and spatial distributions on nanosized oxide minerals.

DISCUSSION

We have performed nanoscale IR imaging and force nanospectroscopy measurements of water films grown on individual mineral nanoparticles. Our imaging and molecular simulations revealed the anisotropic growth of water films within the confines of a single face of a mineral nanoparticles. The driving factors of this anisotropy involve heterogeneous distributions of capture zones for water on mineral surfaces and the high surface tension of water. These findings validate previous concerns for theoretical frameworks predicting layer-by-layer growth (*8*, *37*).

Defects at stepped edges of gibbsite account for a preferential accumulation of water at low RH over other types of defects on the basal face. Simulations at low water loadings suggest a dehydration of flat areas with grooves filled with water films. This supports our imaging efforts revealing the preferential accumulation of water in the form of thick films and even menisci over defects. Further growth in the condensation regime produces thicker films in the middle of

Downloaded from http://advances.sciencemag.org/ on August 13, 2020

a face than at edges. The high surface tension of water is responsible for smoothing the film surface over the particle surface. Because of the inability of theoretical adsorption models in predicting the forms of water films associated to mineral surfaces (*8*, *37*), our imaging and computational work provides the foundation for determining which types of refinements should be most physically justified and important to incorporate in future models.

Our imaging approach to visualize water film growth in situ is uniquely important because our findings would simply not be possible through ex situ methods, low-resolution (optical, scanning electron microscopy, or x-ray) techniques, or solely topographical (AFM) imaging. Recognition of nanoscale topography and surface tension–guided water growth is of significant interest to the geochemical, biomineral, atmospheric materials, geoengineering, and chemical researchers to understand processes controlled by mineral surface topology and water film physicochemistry. The concept of anisotropic water uptake established in our work is widely applicable and is expected to open new possibilities for explaining key exchange and catalytic phenomena involving water films at the nanoscale. In addition, we anticipate that IR *s*-SNOM imaging at vibrational frequencies tuned to those of adsorbed compounds will shed new light on reaction hotspots. Moving onto this area is urgently needed to explain film-mediated reactions especially under conditions of low RH where the existence of water-filled defects was previously not well identified. Recognition of such possibilities will be greatly beneficial for the advancement knowledge of (biogeo)chemical processes in nature and technology.

MATERIALS AND METHODS

Sample preparation for imaging

Synthetic gibbsite (*38*) nanoparticles (44 m^2/g) were suspended in doubly distilled deionized water, and the solution was sonicated for 30 min and then dropcasted on template-stripped gold substrate (Platypus Technologies, product no. AU.1000.SWTSG) for IR *s*-SNOM and AFM studies. Water was evaporated under a stream of dry N_2(g) at 25°C.

Water vapor adsorption isotherm by microgravimetry and modeling

Water vapor adsorption isotherms were collected on gibbsite particles at 25°C by quartz crystal microbalance (QCM). A gold-coated quartz resonator operating at 10 MHz was used for QCM measurements (eQCM 10M, Gamry Instruments Inc.). Changes in frequency (Δf) of the quartz resonator were converted to changes in sample mass (Δm) resulting from water vapor binding using the Sauerbrey equation

$$\Delta f = -\frac{2f_0^2}{A\sqrt{\rho_q \mu_q}}\Delta m \quad (1)$$

In this equation, f_0 is the resonant frequency of empty cell, A is the piezoelectrically active crystal area of the gold-coated quartz crystal (0.205 cm^2), ρ_q is the density quartz (2.648 g/cm^3), and μ_q is shear modulus of quartz (2.947×10^{11} $g/cm{\cdot}s^2$). We chose the serial resonance frequency (f_s) of the quartz resonator to monitor mass, while the parallel resonator frequency was used to ensure that the gibbsite overlayer had sufficient flexibility during the course of the experiment.

The serial resonance frequency of the quartz resonator exposed to a flow of 200 standard cubic centimeters per minute (sccm) dry N_2(g) was first measured to obtain the correct baseline of the empty cell. A dilute aqueous suspension of gibbsite nanoparticles was then sprayed onto the gold area of the resonator and then dried under the same flow of N_2(g). The resulting f_s was used to obtain the mass of the dry sample (11 μg). An adsorption isotherm experiment was thereafter initiated by exposing the sample to water vapor pressures from 0 to 60% RH. The samples were equilibrated for 60 min at each preselected levels of humidity, during which time f_s was monitored. This allowed the sample to reach a time-independent mass representing water loadings achieved at equilibrium prior changing the water vapor pressure. A mass flow controller (MKS, 179A) was used to mix and control the gas flow of N_2(g) and water-saturated N_2(g). The moisture content of the gases was continuously verified by nondispersible IR analysis (LI-7000, LI-COR Inc.).

Adsorption isotherms shown in Fig. 1B were modeled using an adaptation of the model of Do *et al.* (*9*). This model decomposes adsorption isotherms into an adsorption regime at low RH and a condensation regime at high RH. Our adaptation of the model treats adsorption as the formation of the first few more tightly gibbsite-bound water monolayers and condensation as the growth of thick water overlayers and interparticle pore-filling via water-water interactions. The total water uptake (C_μ) is given by

$$C_\mu = S_0\frac{K_f\sum_1^{n=\beta+1} n\cdot p/{p_0}^n}{1+K_f\sum_1^{n=\beta+1} p/{p_0}^n} + C_{\mu s}\frac{K_\mu\sum_1^{n=\alpha+1} p/{p_0}^n}{K_\mu\sum_1^{n=\alpha+1} p/{p_0}^n + \sum_1^{n=\alpha+1} p/{p_0}^{n-\alpha}} \quad (2)$$

as a function of % RH, here expressed in terms of the ratio of the partial pressure of water (p) to the saturation water pressure (p_0 = 3.169 kPa) at 25°C. The left-hand term is a Brunauer-Emmett-Teller–type term for the adsorption regime and the right-hand term to the condensation regime. Parameters for each regime include water-binding sites densities (S_0 = 25 sites/nm^2; $C_{\mu s}$ = 800 sites/nm^2), association constants (K_f = 17; K_μ = 1.5), and hydration numbers (β = 3; α = 4). The latter numbers are fixed, with β = 3 for the adsorption regime denoting that a (hydr)oxo group can be involved in three (donating and/or accepting) hydrogen bonds. This is an average hydration number that we retrieved in previous molecular modeling of water adsorption on various metal (oxy)hydroxides. The other hydration number was optimized to α = 4 for the condensation regime to denote the nominal population of a water nanocluster needed for the water condensation at the mineral surface. We have provided the raw data for the microgravimetry experiments on gibbsite minerals.

FTIR spectroscopy

FTIR spectra of water films bound to gibbsite (fig. S2) were made using an attenuated total reflectance accessory equipped with a diamond optical cell (Golden Gate, Specac). Gibbsite was deposited on the diamond optical cell as an aqueous paste, which was then dried under a stream of N_2(g) in a flow-through lid enabling passage of gases of controlled composition. The dry sample was then exposed to water vapor in the 0 to 75% RH with a 60-min equilibration period at each preselected value of RH and during which time the spectra were collected. These measurements ensured that equilibrium was reached with respect to water binding prior changing the RH of the flowing gas. Spectral lines of unbound water vapor were not detected in this setup, as the gibbsite film covering the diamond optical cell was sufficiently thick to isolate the optical path from the gas phase.

Downloaded from http://advances.sciencemag.org/ on August 13, 2020

These spectral lines were, however, collected in transmission measurements of water vapor uptake on the gibbsite (fig. S3) to identify the absorption lows, where IR *s*-SNOM measurements could be performed (e.g., 1630 cm^{-1}).

All spectra were collected in the spectral range of 600 to 4000 cm^{-1} at a resolution of 4 cm^{-1} with a forward/reverse scanning rate of 10 Hz with a Vertex 70/v FTIR spectrometer (Bruker). In all cases, the Blackman-Harris three-term apodization function with 16 cm^{-1} phase resolutions and the Mertz phase correction algorithm were used to generate FTIR spectra. Each spectrum was obtained from 100 scans, each collected over an 89-s period. We have provided all the raw data for the bulk FTIR studies.

IR *s*-SNOM on single gibbsite nanoparticles

IR *s*-SNOM experiments were performed using an Attocube AFM coupled to continuous wave IR excitation source using a Daylight Solutions MIRcat QCL tunable from 1450 to 1700 cm^{-1} with a bandwidth of <1 cm^{-1} and spectral resolution of 0.25 cm^{-1} (Fig. 2A). The IR laser was focused to AFM tip apex with a parabolic mirror (Numerical aperture of 0.25 and power < 10 mW). All the IR *s*-SNOM measurements were performed with the same laser power at tuned laser wave numbers. The IR *s*-SNOM tips were conductive PtSi (PtSi-NCH, Nanosensors) with a radius of ~25 nm and operated in tapping mode at a resonance frequency of $\omega_t \sim 330$ kHz.

The tip-scattered IR radiation was measured in a two-phase (Φ_1 and Φ_2 in Fig. 2A) homodyne amplification and in detection mode with a HgCdTe detector (Kolmar Technologies). The far-field background was suppressed by demodulating the detected signal at the second or third harmonic of the cantilever oscillation frequency of $2\omega_t$ (Fig. 2D) or $3\omega_t$ (figs. S6 and S7) and sideband modulation (fig. S8) at $2\omega_t + \Omega_r$ (where Ω_r is the frequency of the chopper used in the reference arm, $\Omega_r << \omega_t$) (*25*). For the signal demodulations, we have used a lock-in amplifier from Zürich Instruments (HF2LI). The abovementioned modulation schemes isolated the near-field signal and provided the background-free near-field phase φ, which was used to generate water adsorption images on gibbsite.

The signal from the gold was at least 5 to 10 times lower than that of gibbsite, thus ensuring a high signal-to-noise ratio. Raster scanned *s*-SNOM images were acquired with a lock-in time constant of ~10 ms/pixel for each image with 128 pixels by 128 pixels for IR *s*-SNOM. Before starting repetitive IR *s*-SNOM measurements, higher-resolution topography images (at least 256 pixels by 256 pixels) were taken with the same SNOM system to record the location of the nanoparticles. These initial locations were used as a feedback to minimize sample drift during the repetitive scans needed to map the gibbsite surface exposed to water vapor. All IR *s*-SNOM analyses and statistics were performed using Gwyddion software (*39*).

The IR *s*-SNOM system and the interferometer were encased in a plexiglass box of controlled atmospheric composition. In this setup, water vapor binding was initiated by exposing the gibbsite particles to atmospheres of 0 to 25% RH made by mixing a source of water saturated N_2(g) with dry N_2(g) at different flow rates. Water vapor pressures were monitored continuously using a humidity detector (Omega, OM-73 Humidity Logger) placed inside the SNOM box close to sample holder. For the IR *s*-SNOM experiments, RH values were kept at ≤25% RH to remain under the adsorption regime.

In a separate set of experiments, we also performed QCL spectroscopy by tuning the IR laser in the region of the bending mode of water from 1580 to 1700 cm^{-1}. SNOM images of a 50 pixel–by–50 pixel square region in the center of gibbsite nanoparticle exposed to ambient atmospheric conditions (see black square in fig. S6) were collected for these measurements. The images collected at different wave numbers (fig. S6) were then used to extract the spectrum of Fig. 2B (blue dots). IR *s*-SNOM phase statistics on the mineral were extracted with respect to gold substrate using Gwyddion (*39*). Mean values represent water binding on gibbsite, and standard deviations represent changes in those values.

IR s-SNOM on single holmium oxide nanoparticles

Hydrophobic holmium oxide (Ho_2O_3) nanoparticles (Sigma-Aldrich, product no. 229679) were imaged to test for adventitious condensation during IR *s*-SNOM imaging (fig. S9). Azimi *et al.* (*24*) showed that Ho_2O_3 and other rare earth oxides are more hydrophobic because of the electronic configuration of the metal ions, disfavoring Lewis acid-type metal-water binding. In these measurements, we used both sideband modulation at $2\omega_t + \Omega_r$ (where Ω_r is the frequency of the chopper used in the reference arm, $\Omega_r << \omega_t$) (*25*) and second harmonic demodulation ($2\omega_t$) (fig. S9). Both $2\omega_t$ and $2\omega_t + \Omega_r$ showed significantly low water absorption in our IR *s*-SNOM phase images (Fig. 3A and fig. S9) compared to gibbsite (Fig. 2D and figs. S4 and S6 to S8).

IR *s*-SNOM data analysis

Near-field phase properties of gibbsite nanoparticles, which correspond to nanoscale IR absorption, were extracted by the two-phase homodyne detection technique. This was achieved by changing the reference arm between two known orthogonal phase components (Φ_1 and Φ_2 and where $\Phi_1 = \Phi_2 + \pi/2$; see Fig. 2A for reference arm mirror). Intensities were obtained from the phase values with (*25*)

$$I_1 = A\cos(\Phi - \Phi_1), \text{ using } \Phi_1 = \Phi_2 + \pi/2 \quad (3)$$

$$I_2 = A\cos(\Phi - \Phi_2) = A\sin(\Phi - \Phi_1) \quad (4)$$

Gwyddion (*39*) was used to extract the near-field phase with $\varphi_{NF} = \arctan(I_1/I_2)$. The φ_{NF} function represents a measure of water adsorption on gibbsite. For comparison of SNOM phase images at different RH, the recorded mineral signals were rescaled with respect to the gold substrate, thus treating the gold substrate as the background.

The integrated SNOM phase values of Fig. 3 (A and B) were obtained by a numerical integration over the area of the gibbsite particle identified by SNOM topography. These calculations were achieved counting the SNOM phase value over every pixel where the SNOM topography exceeds 1 nm over the average and numerically leveled topography of the supporting gold substrate. The integrated phase values were normalized for the particle surface area, hence the unit $\Sigma\varphi/\mu m^2$ in Fig. 3 (A and B). These numerical analyses were performed in the computational environment of MATLAB (The MathWorks Inc.). We have provided all the raw data (I_1, I_2) and the calculated data for the near-field phase images for the SNOM measurements.

AM-AFM on single gibbsite nanoparticles

AM-AFM imaging and force-distance curves were obtained using a Cypher ES (Asylum Research), equipped with a temperature-controlled Peltier stage, and an ARROW-UHFAuD silicon probe (NanoWorld) with nominal radius of less than 10 nm. The probe spring constant was estimated using GetReal automated calibration at 5.5 N/m, and the cantilever resonance frequency was 1.04 MHz. Images were collected in amplitude-modulated imaging mode using BlueDrive

Downloaded from http://advances.sciencemag.org/ on August 13, 2020

optical actuation with free amplitudes of 5.2 to 7.0 Å and amplitude set points at ~80% of the free amplitude. Initial images were collected on several particles to examine the range of defects and spiral growth features manifested in the sample (fig. S1). During experimental acquisition, the sample chamber was initially purged with dry Ar(g). Water vapor deposition was initiated by exposing gibbsite particles to a stream of humidified Ar(g) (~40% RH at room temperature), prepared by sparging Ar(g) through a 49% (w/w) solution of room temperature (25°C) $CaCl_2{\cdot}H_2O$ in Milli-Q water. The partial pressure of the gas phase was verified by nondispersible IR analysis (LI-7000, LI-COR Inc.).

Images obtained while flowing the humidified Ar(g) over gibbsite at 30°C showed no significant difference from those obtained under dry Ar(g). RH at the sample surface was subsequently increased by maintaining argon flow and reducing the sample temperature using the Peltier cooler, until evidence of water films was seen at 10° and 4°C. Precise RH values were seen to vary within the sample chamber, as evidenced by visible droplets of water condensation forming on the gold substrate at 4°C (fig. S11). These droplets were, however, suppressed near the AFM probe, suggesting that the local RH is reduced by local heating in the vicinity of the AFM probe. We have provided all the raw and processed data for AFM imaging studies.

AFM amplitude-distance measurements

At the subnanometer scale, AM-AFM contrast formation mechanisms can be complex (*29*, *32*). Thus, we collected a series of amplitude-modulated force curves at each temperature and humidity condition. These provide insights into the sample-tip interaction forces (*33*) and present additional evidence that the apparent changes in particle thickness are due to the formation of a water film. At each condition of interest, between 80 and 200 force-distance curves were obtained at several locations on top of the gibbsite particle, and a similar number of curves were collected at several locations over the neighboring gold substrate. All curves were obtained using driven cantilevers with free amplitudes ranging from 5.2 to 7.0 Å while monitoring amplitude, phase, and deflection. A selection of representative curves is shown in figs. S12 to S14 for one site at each condition. For each individual curve, the jump-to-contact (on approach) or jump-from-contact (on retract) was determined by identifying the jump in the amplitude-distance plot. A representative average curve for each site and condition was obtained by calculating an average curve in the in-contact regime (Z less than jump distance) and in the away-from contact regime (Z greater than jump distance) and by connecting these curves at the average jump distance for that site and condition. Average distances of jump-to-contact and jump-from-contact are reported in table S1 and Fig. 4E. To ensure consistent contact with the sample, a deflection-based approach-retract set point was used with the distance of closest approach ($Z = 0$) corresponding to nominal contact force of ~2 nN. We have provided all the raw data for the AFM force curve measurements.

Classical MD simulations of water films on a single gibbsite nanoparticles

The spatial distribution of water bound on pristine and roughened surfaces of a single gibbsite nanoparticle was simulated by classical MD. A 11.2 nm by 13.4 nm by 4.7 nm single hexagonal gibbsite particle was cut from a crystal along the (001) basal and (101) edge faces. This size was chosen for computational efficiency, and the crystal habit was made slightly asymmetric as in the particles studied experimentally.

Undersaturated surface Al sites were coordinated with hydroxyl to produce 1610 doubly coordinated hydroxo (μ-OH; ≡ Al_2-OH^0) groups for each of the two (001) and 80 singly coordinated hydroxo groups (-OH; ≡ Al-$OH^{0.5-}$) on each of the six (101) faces. The remaining sites of the (101) are Lewis acid sites (≡ $Al^{0.5+}$) available for direct water binding. The partial charges on these sites are estimated from the Pauling valence, and the protonation state of the sites accounts for the surface charge of each crystallographic face of the simulated particle, all of which were zero. The composition of resulting neutrally charge pristine particle was $Al_{9819}(OH_{bulk})_{25745}(OH_{surface})_{3712}$. One of the (001) faces of this particle was then roughened by cutting from the middle of the basal face to one side over a depth of three atomic steps (~0.5 nm per step). Three grooves of up to ~1.0 nm deep were thereafter made along this new face. The composition of the resulting neutrally charged particle was $Al_{8631}(OH)_{22021}(OH_{surface})_{3872}$. This particle was terminated by a greater diversity of singly, doubly, and triply coordinated hydroxo functional groups with underlying Al ions. The resulting simulation cells were placed in the center of a 20 nm–by–20 nm–by–20 nm box.

The single gibbsite particle surfaces were covered by films of homogeneous thickness with loadings of 3, 12, 21, and 33 H_2O/nm^2. This was achieved using the gmx solvate utility of GROMACS/2018.3 (*40*). Classical MD simulations (300 K) as described in our previous work on aluminum oxides (*4*) were carried out using the revised ClayFF force field for gibbsite and water (*41*). Simulation cells were first energy-minimized (double precision) using a steepest descent algorithm. The minimized structure was then equilibrated (single precision) using classical MD for at least 10^7 steps (5000 ps at 0.5-fs time step), followed by production runs of at least another 5000 ps. Total energy convergence and its components as well as temperature and atomic densities were monitored for these entire equilibration periods. This modeling strategy adequately reproduced the ideal bulk gibbsite structure. Although a certain extent of surface relaxation is to be noted, the relative positions of all top Al and O atoms in all slabs and in the particle remained in place throughout the course of all simulations and represent the crystallographic terminations of gibbsite.

SUPPLEMENTARY MATERIALS

Supplementary material for this article is available at http://advances.sciencemag.org/cgi/content/full/6/30/eaaz9708/DC1

REFERENCES AND NOTES

1. G. E. Ewing, Ambient thin film water on insulator surfaces. *Chem. Rev.* **106**, 1511–1526 (2006).
2. M. Kim, D. Or, Microscale pH variations during drying of soils and desert biocrusts affect HONO and NH_3 emissions. *Nat. Commun.* **10**, 3944 (2019).
3. G. Rubasinghege, V. H. Grassian, Role(s) of adsorbed water in the surface chemistry of environmental interfaces. *Chem. Commun.* **49**, 3071–3094 (2013).
4. J.-F. Boily, L. Fu, A. Tuladhar, Z. Lu, B. A. Legg, Z. M. Wang, H. Wang, Hydrogen bonding and molecular orientations across thin water films on sapphire. *J. Colloid Interface Sci.* **555**, 810–817 (2019).
5. R. Tecon, A. Ebrahimi, H. Kleyer, S. E. Levi, D. Or, Cell-to-cell bacterial interactions promoted by drier conditions on soil surfaces. *Proc. Natl. Acad. Sci. U.S.A.* **115**, 9791–9796 (2018).
6. P. J. DeMott, A. J. Prenni, X. Liu, S. M. Kreidenweis, M. D. Petters, C. H. Twohy, M. S. Richardson, T. Eidhammer, D. C. Rogers, Predicting global atmospheric ice nuclei distrubitions and their impacts on climate. *Proc. Natl. Acad. Sci. U.S.A.* **107**, 11217–11222 (2010).
7. M. G. Lawrence, S. Schäfer, H. Muri, V. Scott, A. Oschlies, N. E. Vaughan, O. Boucher, H. Schmidt, J. Haywood, J. Scheffran, Evaluating climate geoengineering proposals in the context of the Paris Agreement temperature goals. *Nat. Commun.* **9**, 3734 (2018).

Downloaded from http://advances.sciencemag.org/ on August 13, 2020

8. M. Tang, D. J. Cziczo, V. H. Grassian, Interactions of water with mineral dust aerosol: Water adsorption, hygroscopicity, cloud condensation, and ice nucleation. *Chem. Rev.* **116**, 4205–4259 (2016).
9. D. D. Do, S. Junpirom, H. D. Do, A new adsorption–desorption model for water adsorption in activated carbon. *Carbon* **47**, 1466–1473 (2009).
10. N. G. Petrik, P. L. Huestis, J. A. La Verne, A. B. Aleksandrov, T. M. Orlando, G. A. Kimmel, Molecular water adsorption and reactions on α-Al_2O_3(0001) and α-alumina particles. *J. Phys. Chem. C* **122**, 9540–9551 (2018).
11. S. Santos, A. Verdaguer, Imaging water thin films in ambient conditions using atomic force microscopy. *Materials* **9**, 182 (2016).
12. K. Xu, P. Cao, J. R. Heath, Graphene visualizes the first water adlayers on mica at ambient conditions. *Science* **329**, 1188–1191 (2010).
13. J. Hu, X.-D. Xiao, D. F. Ogletree, M. Salmeron, Imaging the condensation and evaporation of molecularly thin films of water with nanometer resolution. *Science* **268**, 267–269 (1995).
14. S. Maier, M. Salmeron, How does water wet a surface? *Acc. Chem. Res.* **48**, 2783–2790 (2015).
15. L. Xu, A. Lio, J. Hu, D. F. Ogletree, M. Salmeron, Wetting and capillary phenomena of water on mica. *J. Phys. Chem. B* **102**, 540–548 (1998).
16. Y.-H. Lu, J. M. Larson, A. Baskin, X. Zhao, P. D. Ashby, D. Prendergast, H. A. Bechtel, R. Kostecki, M. Salmeron, Infrared nanospectroscopy at the graphene–electrolyte interface. *Nano Lett.* **19**, 5388–5393 (2019).
17. B. L. Weeks, M. W. Vaughn, J. J. DeYoreo, Direct imaging of meniscus formation in atomic force microscopy using environmental scanning electron microscopy. *Langmuir* **21**, 8096–8098 (2005).
18. M. Bartošík, L. Kormoš, L. Flajšman, R. Kalousek, J. Mach, Z. Lišková, D. Nezval, V. Švarc, T. Šamořil, T. Šikola, Nanometer-sized water bridge and pull-off force in AFM at different relative humidities: Reproducibility measurement and model based on surface tension change. *J. Phys. Chem. B* **121**, 610–619 (2017).
19. I. Siretanu, D. van den Ende, F. Mugele, Atomic structure and surface defects at mineral-water interfaces probed by in situ atomic force microscopy. *Nanoscale* **8**, 8220–8227 (2016).
20. A. Klaassen, F. Liu, D. van den Ende, F. Mugele, I. Siretanu, Impact of surface defects on the surface charge of gibbsite nanoparticles. *Nanoscale* **9**, 4721–4729 (2017).
21. M. Yeşilbaş, J.-F. Boily, Particle size controls on water adsorption and condensation regimes at mineral surfaces. *Sci. Rep.* **6**, 32136 (2016).
22. W. Thomson, On the equilibrium of vapour at a curved surface of liquid. *Philos. Mag.* **42**, 448–452 (1871).
23. E. A. Muller, B. Pollard, M. B. Raschke, Infrared chemical nano-imaging: Accessing structure, coupling, and dynamics on molecular length scales. *J. Phys. Chem. Lett.* **6**, 1275–1284 (2015).
24. G. Azimi, R. Dhiman, H.-M. Kwon, A. T. Paxson, K. K. Varanasi, Hydrophobicity of rare-earth oxide ceramics. *Nat. Mater.* **12**, 315–320 (2013).
25. S. Berweger, D. M. Nguyen, E. A. Muller, H. A. Bechtel, T. T. Perkins, M. B. Raschke, Nano-chemical infrared imaging of membrane proteins in lipid bilayers. *J. Am. Chem. Soc.* **135**, 18292–18295 (2013).
26. G. Dominguez, A. S. Mcleod, Z. Gainsforth, P. Kelly, H. A. Bechtel, F. Keilmann, A. Westphal, M. Thiemens, D. N. Basov, Nanoscale infrared spectroscopy as a non-destructive probe of extraterrestrial samples. *Nat. Commun.* **5**, 5445 (2014).
27. I. T. Lucas, A. S. McLeod, J. S. Syzdek, D. S. Middlemiss, C. P. Grey, D. N. Basov, R. Kostecki, IR near-field spectroscopy and imaging of single Li_xFePO_4 microcrystals. *Nano Lett.* **15**, 1–7 (2014).
28. M. A. Holden, T. F. Whale, M. D. Tarn, D. O'Sullivan, R. D. Walshaw, B. J. Murray, F. C. Meldrum, H. K. Christenson, High-speed imaging of ice nucleation in water proves the existence of active sites. *Sci. Adv.* **5**, eaav4316 (2019).
29. R. García, *Amplitude Modulation Atomic Force Microscopy* (John Wiley & Sons, 2011).
30. A. Checco, Y. Cai, O. Gang, B. M. Ocko, High resolution non-contact AFM imaging of liquids condensed onto chemically nanopatterned surfaces. *Ultramicroscopy* **106**, 703–708 (2006).
31. A. Méndez-Vilas, A. B. Jódar-Reyes, M. L. González-Martín, Ultrasmall liquid droplets on solid surfaces: Production, imaging, and relevance for current wetting research. *Small* **5**, 1366–1390 (2009).
32. P. Rahe, R. Bechstein, J. Schütte, F. Ostendorf, A. Kühnle, Repulsive interaction and contrast inversion in noncontact atomic force microscopy imaging of adsorbates. *Phys. Rev. B* **77**, 195410 (2008).
33. A. F. Payam, D. Martin-Jimenez, R. Garcia, Force reconstruction from tapping mode force microscopy experiments. *Nanotechnology* **26**, 185706 (2015).
34. M. H. Factorovich, V. Molinero, D. A. Scherlis, Vapor pressure of water nanodroplets. *J. Am. Chem. Soc.* **136**, 4508–4514 (2014).
35. B. Rotenberg, A. J. Patel, D. Chandler, Molecular explanation for why talc surfaces can be both hydrophilic and hydrophobic. *J. Am. Chem. Soc.* **133**, 20521–20527 (2011).
36. J.-F. Boily, M. Yeşilbaş, M. M. M. Uddin, L. Baiqing, Y. Trushkina, G. Salazar-Alvarez, Thin water films at multifaceted hematite particle surfaces. *Langmuir* **31**, 13127–13137 (2015).
37. C. D. Hatch, P. R. Tumminello, M. A. Cassingham, A. L. Greenaway, R. Meredith, M. J. Christie, Technical note: Frenkel, Halsey and Hill analysis of water on clay minerals: Toward closure between cloud condensation nuclei activity and water adsorption. *Atmos. Chem. Phys.* **19**, 13581–13589 (2019).
38. X. Zhang, P. L. Huestis, C. I. Pearce, J. Z. Hu, K. Page, L. M. Anovitz, A. B. Aleksandrov, M. P. Prange, S. Kerisit, M. E. Bowden, W. Cui, Z. Wang, N. R. Jaegers, T. R. Graham, M. Dembowski, H.-W. Wang, J. Liu, A. T. N'Diaye, M. Bleuel, D. F. R. Mildner, T. M. Orlando, G. A. Kimmel, J. A. La Verne, S. B. Clark, K. M. Rosso, Boehmite and gibbsite nanoplates for the synthesis of advanced alumina products. *ACS App. Nano Mater.* **1**, 7115–7128 (2018).
39. D. Nečas, P. Klapetek, Gwyddion: An open-source software for SPM data analysis. *Centr. Eur. J. Phys.* **10**, 181–188 (2012).
40. D. Van Der Spoel, E. Lindahl, B. Hess, G. Groenhof, A. E. Mark, H. J. C. Berendsen, GROMACS: Fast, flexible, and free. *J. Comput. Chem.* **26**, 1701–1718 (2005).
41. M. Pouvreau, J. A. Greathouse, R. T. Cygan, A. G. Kalinichev, Structure of hydrated gibbsite and brucite edge surfaces: DFT results and further development of the ClayFF classical force field with metal–O–H angle bending terms. *J. Phys. Chem. C* **121**, 14757–14771 (2017).

Acknowledgments: We thank S. Lea for access to the IR s-SNOM system and support throughout this study, and J. D. Yoreo for access to AM-AFM capabilities and for advice on nanoscale imaging. We also thank them for their critical reading of the manuscript. We thank M. Raschke and J. Atkin for advice on IR *s*-SNOM system development, T. Gokus from Neaspec GmbH for technical assistance with nanoscale IR imaging, and X. Zhang for providing gibbsite nanoparticles. We also thank L. Kovarik, E. Martz, and P. Dahl for helpful discussions. **Funding:** This work was supported by the Swedish Research Council to J.-F.B. (2016-03808). All IR *s*-SNOM work was performed at the Environmental Molecular Sciences Laboratory (EMSL) (Ringgold ID 130367), a DOE Office of Science User Facility sponsored by the Office of Biological and Environmental Research, and under the user project (49764) to J.-F.B. AM-AFM experiments were partially supported BES Division of Materials Science and Engineering, Synthesis and Processing Sciences Program, and were performed at Pacific Northwest National Laboratory, a multiprogram national laboratory operated for the DOE by Battelle under Contract No. DE-AC05-76RL01830. This research was partially supported by the NIH Director's New Innovator award (1DP2AI138259-01 to N.S.M.) and NSF CAREER award no. 1749662 (to N.S.M.). Research was sponsored by the Defense Advanced Research Projects Agency (DARPA) Army Research Office (ARO) and was accomplished under Cooperative Agreement Number W911NF-18-2-0100 (with N.S.M.). Research in the Malvankar laboratory is also supported by the Career Award at the Scientific Interfaces from Burroughs Wellcome Fund (to N.S.M.), the Charles H. Hood Foundation Child Health Research Award, and the Hartwell Foundation Individual Biomedical Research Award. **Author contributions:** S.E.Y. and J.-F.B. conceived and designed the study, and J.-F.B. supervised the project. S.E.Y. built the QCL-coupled IR *s*-SNOM detection interferometer, prepared gibbsite samples, performed IR nanospectroscopy measurements on individual particles, and analyzed the data. B.A.L. performed AM-AFM imaging and force spectroscopy studies with S.E.Y. and analyzed the data. M.Y. performed microgravimetric and FTIR spectroscopic water vapor adsorption isotherms and analyzed the data. N.S.M. guided the measurements and helped to interpret the data. J.-F.B. performed adsorption isotherm modeling and integrated SNOM phase calculations, and MD simulations. J.-F.B., S.E.Y., and N.S.M. cowrote the article with inputs from all authors. **Competing interests:** The authors declare that they have no competing interests. **Data and materials availability:** All raw data needed to evaluate the conclusions in the paper are present in the paper and/or the Supplementary Materials. Additional data related to this paper may be requested from the authors.

Submitted 29 October 2019
Accepted 10 June 2020
Published 24 July 2020
10.1126/sciadv.aaz9708

Citation: S. E. Yalcin, B. A. Legg, M. Yeşilbaş, N. S. Malvankar, J.-F. Boily, Direct observation of anisotropic growth of water films on minerals driven by defects and surface tension. *Sci. Adv.* **6**, eaaz9708 (2020).

Downloaded from http://advances.sciencemag.org/ on August 13, 2020

Science Advances

Direct observation of anisotropic growth of water films on minerals driven by defects and surface tension

Sibel Ebru Yalcin, Benjamin A. Legg, Merve Yesilbas, Nikhil S. Malvankar and Jean-François Boily

Sci Adv **6** (30), eaaz9708.
DOI: 10.1126/sciadv.aaz9708

ARTICLE TOOLS http://advances.sciencemag.org/content/6/30/eaaz9708

SUPPLEMENTARY MATERIALS http://advances.sciencemag.org/content/suppl/2020/07/20/6.30.eaaz9708.DC1

REFERENCES This article cites 40 articles, 5 of which you can access for free
http://advances.sciencemag.org/content/6/30/eaaz9708#BIBL

PERMISSIONS http://www.sciencemag.org/help/reprints-and-permissions

Use of this article is subject to the Terms of Service

Science Advances (ISSN 2375-2548) is published by the American Association for the Advancement of Science, 1200 New York Avenue NW, Washington, DC 20005. The title *Science Advances* is a registered trademark of AAAS.

Copyright © 2020 The Authors, some rights reserved; exclusive licensee American Association for the Advancement of Science. No claim to original U.S. Government Works. Distributed under a Creative Commons Attribution NonCommercial License 4.0 (CC BY-NC).

Downloaded from http://advances.sciencemag.org/ on August 13, 2020